Fabrication of Bi_2MoO_6/CdS Heterostructures Nanocomposite: Enhanced Photocatalytic and Photoelectrochemical Performance under Visible-Light Irradiation

Muhammad Arif, Tong Yu, Zhang Min, Qingyong Li, and Xiaoheng Liu

***Abstract*—We employed one dimensional (1D) CdS nanobelt as a synthetic templet and developed Bi_2MoO_6/CdS heterostructures nanocomposite by simple 2 steps hydrothermal method. The as prepared Bi_2MoO_6/CdS heterostructures nanocomposite possess good dispersity and exhibits excellent photocatalytic activity towards rhodamine B (RhB) and phenol under visible light irradiation. Importantly, the large specific surface area of Bi_2MoO_6/CdS heterostructures nanocomposite (52.7 m^2 g^{-1}) and high electron mobility contributes to the enhanced photolytic activity. The as prepared heterostructures nanocomposite also exhibits significant photocatalytic oxygen evolution with rate of 0.773 mmol h^{-1} g^{-1}. A series of experiments validate that the B_3MoO_6/CdS heterostructures nanocomposite contributes to improved photocatalytic activity and the electrons/holes separation are well promoted. Thus, the current research provides an efficient rout for the fabrication of photostable heterostructures nanocomposite with an effective utilization of solar light.**

***Index Terms*—B_2MoO_6/CdS heterostructures nanocomposite, photocatalysis, water oxidation, photoelectochemistry.**

I. Introduction

Semiconductor photocatalysis has been becoming promising technology for solving the major environmental pollution problems and energy crisis [1], [2]. Semiconductor TiO_2 was considered the most efficient photocatalyst because of its potential photocatalytic activity, photostability and nontoxicity [3]. However, the quantum efficiency and the light response range limited the photocatalytic application [4], [5]. Consequently, efficient and promising visible light driven photocatalyst became the major focus of researcher in the field of photocatalysis. In the present time, two basic strategies have been employed to manipulate the above problems: modifying TiO_2 or fabricating new type of semiconductor heterojunction photocatalysts [6], [7].

In the present time, two dimensional (2D) nanoflakes deposited on one dimensional (1D) nanostructured

semiconductor the deposition of two dimensional (2D) nanoflakes on dimension (1D) heterostructured semiconductor to fabricate three dimensional (3D) structure with enhance properties have been efficiently fabricated and exceedingly regarded in countless application in the field of photocatalysis, energy storage materials such as batteries, supercapacitor, solar cells photodetectors and gas sensing, respectively [8]-[10]. Among these one-dimension (1D) semiconductors, Metal sulphides, TiO_2 has been greatly investigated in the present time for their great potential and promising application for H_2, O_2 and solar energy conversion [11]. For example, TiO_2 and ZnS due to their bandgap of 3.2 eV and 3.6 eV absorb in the UV region [12], whereas CdS because of it narrow bandgap of 2.4 eV [13] absorb in the visible region. To further ensure the full spectrum utilization of solar energy, some Bismuth based semiconductor can be incorporated on CdS which can absorb the Visible-NIR radiation.

Bi-based semiconductor photocatalyst, such as Bi_2WO_6, Bi_2O_3, $Bi_4Ti_3O_{12}$ and Bi_2MoO_6 attracted great attention because of their unique layer structure and efficient catalytic and high photostability [14], [15]. Among the Bi-based semiconductor, Bi_2MoO_6 is the mostly reported photocatalyst in waste-water treatment, air pollution and O_2 evaluation [16]-[18]. Particularly, Bi_2MoO_6 is an n-type aurivillius semiconductor with bandgap energy of 2.7 eV, is one of the promising visible light driven photocatalyst [19]. However, due to its flat band potential and low charge carrier mobility on whichever valence or conduction band, Bi_2MoO_6 limited its application. Eventually, causing faster electron-hole recombination before absorbed on the species and generate oxidative ions. Furthermore, Bi_2MoO_6 only can absorb irradiation below 460 nm to trigger the photocatalysis process. To improve the absorption of visible light driven capacity for Bi_2MoO_6 is another issue. Recently, many approaches have been carried out, such as doping of metal/non-metal [20], [21] and coupling of Bi_2MoO_6 with other narrow band gap semiconductors [22], [23]. The establishment of heterostructures between Bi_2MoO_6 and other semiconductor may improve the photocatalysis efficiency of Bi_2MoO_6 through hindering the recombination of photogenerated charge carriers by built-in electric field [24], [25].

CdS is a narrow band gap semiconductor with band gap energy of 2.4 eV can absorb visible light at a wavelength of 520 nm and is a promising semiconductor photocatalyst for detoxification of pollutants and H_2 evaluation, respectively [26], [27]. However, pure CdS suffered some shortcomings, such as photocorrosion under visible light illumination and fast recombination of photogenerated electron-hole pairs [28], [29]. To overcome such drawbacks, CdS is mostly used as the component of semiconductor heterojunctions. As might be expected, the heterojunction of Bi_2MoO_6 and CdS plays a critical role in Bi_2MoO_6/CdS heterostructured semiconductor: a suitable conduction band edge of Bi_2MoO_6 (-0.32 V vs.

Manuscript received September 19, 2018; revised November 21, 2018.

All Authors are associated with: Key Laboratory for Soft Chemistry and Functional Materials of Ministry of Education, School of Chemical Engineering, Nanjing University of Science and Technology, China (e-mail: xhliu@njust.edu.cn, wazir.chemist@yahoo.com, 15150582969@163.com).

doi: 10.18178/ijcea.2018.9.6.728

NHE) [30] which can react with O_2 to yield $^{\bullet}O_2^-$ and Bi_2MoO_6 nanosheets will provide more surface for reaction sites. Moreover, there are rare reports on Bi_2MoO_6 and CdS heterostructures for O_2 evaluation.

In this work, we hydrothermally synthesized of Bi_2MoO_6/CdS heterostructures nanocomposite using CdS nanowires as 1D nanoscale substrate. The 1D CdS nanowires provided precise and uniform growth for Bi_2MoO_6 in Bi_2MoO_6/CdS heterostructures nanocomposite photocatalyst. The photocatalytic activity and photostability of Bi_2MoO_6/CdS have been investigated for the photo-decomposition of rhodamine B, phenol and photocatalytic O_2 evaluation. Furthermore, the photoelectro- chemical performance and precise photocatalytic mechanism of Bi_2MoO_6/CdS heterostructures nanocomposite were also discussed.

II. Experimental Section

A. Materials and Reagents

All the chemicals (AR grade) used in this work, are cadmium nitrate tetrahydrate $Cd(NO_3)_2.4H_2O$, thiourea, ethylenediamine, ethylene glycol, bismuth nitrate pentahydrate ($Bi(NO_3)_3.5H_2O$), sodium molybdate dihydrate ($Na_2MoO_4.2H_2O$), ethanol, acetone and distilled water. All the chemicals were pure and used without further purification.

B. Preparation of CdS Nanobelts

The CdS nanobelts were prepared by hydrothermal method as reported in the literature with a slight modification [31]. Briefly, $Cd(NO_3)_2.4H_2O$ (0.641 g) and thiourea (0.474 g) were added into a 50 ml Teflon-lined stainless-steel autoclave. After that, 25 ml of ethylenediamine were added and the autoclave were sealed and heated for 72 h at 180 °C. After completion of hydrothermal reaction time, the autoclave was suddenly quenched to room temperature. The yellow precipitate obtained were centrifuged, washed several times with ethanol, water and then dried in a vacuum oven for 12 h at 60 °C.

C. Preparation of Bi_2MoO_6/CdS Nanobelts Heterostructures Nanocomposite

The Bi_2MoO_6/CdS heterostructures nanocomposite with different mole ratios were synthesized by coprecipitation hydrothermal technique. Briefly, 0.4 mmol (0.4-1.6 mmol) of $Bi(NO_3)_3.5H_2O$ and 0.2 mmol (0.2-0.8 mmol) of $Na_2MoO_4.2H_2O$ were ultrasonically dispersed in 20 ml ethylene glycol, respectively. After complete dispersion, the above suspension was then mixed together and 0.2 mmol of CdS nanobelt were then added and again stir for 30 min. The resulting suspension were then added into a 50 ml Teflon-lined stainless-steel autoclave, sealed and maintained at 160 °C for 24 h. Finally, the obtained precipitate was washed several times with ethanol and acetone and collected by centrifugation. The precipitate was then dried in a vacuum oven for 12 h at 60 °C. For comparison, pure Bi_2MoO_6 was prepared by the same method without using CdS nanobelt. The molar ratio of Bi_2MoO_6 to CdS were fixed as 1:1, 2:1, 3:1 and 4:1 and the samples were named as BM for pure Bi_2MoO_6 nanosheet, CD for pure CdS nanobelt, BM-1/CD, BM-2/CD, BM-3/CD and BM-4/CD for Bi_2MoO_6/CdS heterostructures with different mole ratios of Bi_2MoO_6 and CdS. Interestingly, no acid treatment or surfactant used for CdS nanobelt surface roughening before the deposition of Bi_2MoO_6.

D. Characterization

The crystallinity and phase structure of the samples were measured by powder X-ray diffraction (XRD) Bruker advance X-ray diffractometer with Cu Kα radiation (λ= 1.5418 Å) operated at 40 kV and 40 mA. Scanning electron microscopy (SEM) and transmission electron microscopy (TEM) were operated at JOEL-JSM 6360 LV field emission microscopy and JOEL-2100. UV/Vis diffused reflectance (DRS) were operated at Shimadzu UV-2500 with maximum excitation wavelength from 200 nm to 1100 nm using $BaSO_4$ as a reflectance standard. Photoluminescence (PL) spectra of samples were recorded on FL3-TCSPS florescence spectrometer with excitation wavelength from 300 nm to 600 nm using a 5 nm slit. The electrochemical impedance spectra (EIS) and photocurrent were recorded on electrochemical analyzer workstation CHI660A, CH instrument Co, in a standard three electrode system using sample as a working electrode. The X-ray photoelectron spectrometer was operated on PerkinElmer PHI5300 with A1Kα radiation (1=8.4 Å) as an excitation source.

E. Photocatalytic Activity Test

The photocatalytic activity of Bi_2MoO_6/CdS was studied for the photodegradation of RhB, phenol and photocatalytic oxygen evaluation under visible light irradiation (300 W Xe arc lamp at 420 nm with cut off filter to remove light <420 nm). In the photocatalytic degradation of RhB and phenol, 50 mg of catalyst was added into 50 ml (20 gm/L) of RhB and phenol solution, respectively. Prior to irradiation, the solution was stirred and in dark for 30 min to attain the adsorption- desorption equilibrium. Before irradiation and at a given interval of time, a sample of 3 ml was taken from the reaction suspension and centrifuged to remove the catalyst particles. The samples were then analyzed by UV/vis spectrophotometer at an excitation wavelength from 200 nm to 800 nm and the results obtained. In the photocatalytic oxygen evaluation, 0.3 g of photocatalyst was added in 100 ml (0.05 mol/L) of silver nitrate solution. The photocatalytic activity was evaluated by water oxidation using silver nitrate ($AgNO_3$) as an electron scavenger. The samples were first stirred in dark for 30 min to attain the adsorption-desorption equilibrium and then degassed for removal O_2 in solution and air and irradiation under visible light ≥ 420 nm (300 W Xe arc lamp). The amount of oxygen evolved was determined by a gas chromatograph (GC-1690, Jiedao, TCD).

III. Results and Discussion

A. XRD and XPS

Fig. 1 shows the XRD patterns of CdS, Bi_2MoO_6 and Bi_2MoO_6/CdS heterostructures nanocomposite with different

mole ratios of Bi_2MoO_6 and CdS. For pure CdS nanobelt Fig. 1 (curve a), the prominent diffraction peaks observed at 2θ= 24.9°, 26.5°, 28.3°, 36.7°, 43.7°, 47.9°, 50.9°, 51.8°, 52.7°, 66.8°, 71.0° and 75.6° could be perfectly indexed to the (100), (002), (101), (102), (110), (103), (200), (112), (201), (203), (211) and (212) which is the agreement with CdS hexagonal wurtzite structure with lattice parameters *a*= 4.136, *b*= 4.136 and *c*=6.713 (JCPDF= 01-077-2306). It is important to discuss that the relative intensity of (002) peak is remarkably low compared with standard data. It can be concluded that the material is efficiently growing along the *c* axis, which lies parallel to the experimental plane during XRD measurement. Fig. 1 (curve b), the diffraction peak at 2θ= 28.2°, 32.5°, 33.0°, 46.8°, 47.1°, 55.3°, 55.5°, and 56.0° are observed in pure Bi_2MoO_6. These peaks could be indexed to (131), (002), 060), (202), (260), (331), (133) and (191) planes which can be attributed to arthorhombic Bi_2MoO_6 nanosheet (JCPDF= 01-076-2388. For Bi_2MoO_6/CdS heterostructures nanocomposites with different mole ratios of Bi_2MoO_6 and CdS (Fig. 1, curve c, d, e and f), all the observed peaks can be assigned either CdS or Bi_2MoO_6. No further diffraction peaks are observed in the XRD patterns indicating the high purity of the samples.

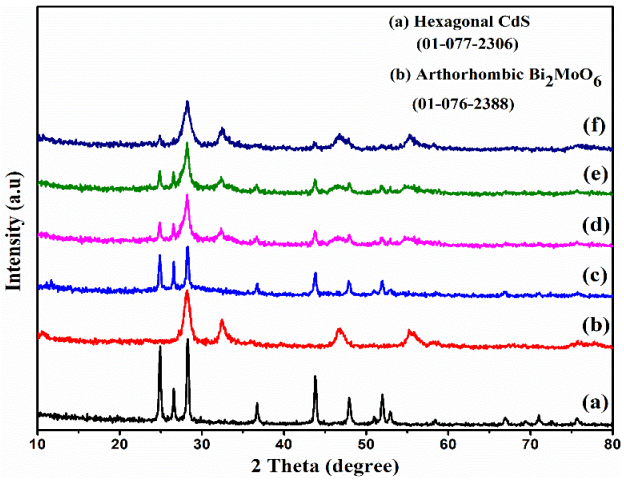

Fig. 1. XRD patterns of (a) CdS nanobelt, (b) Bi_2MoO_6, (c, d, e, f) Bi_2MoO_6/CdS heterostructures nanocomposite with different mole ratios 1:1, 2:1, 3:1, 4:1.

To explain the elemental and chemical states of Bi_2MoO_6/CdS heterostructures nanocomposite, the XPS spectra and high-resolution orbit scan for Bi_2MoO_6/CdS was investigated and the results are depicted and shown in Fig. 2. At first, all the spectra were calibrated, and the binding energy was fixed at 284.6 eV. The XPS survey spectrum (Fig. 2a) for Bi_2MoO_6/CdS heterostructures confirmed the presence of all the elements such as Bi, Mo, O, Cd, and S present in the sample with characteristics peaks; no impurities were observed indicating the high purity of samples. For Bi 4f orbit scan (Fig. 2b), the two-characteristic intense peak detected in spectra at 157.8 eV and 163.1 eV which can be assign to Bi $4f_{7/2}$ and Bi $4f_{5/2}$, respectively [32]. The binding energy peak for Mo 3d orbit scan (Fig. 2c), observed at 231.0 eV and 234.1 eV, can be assign to Mo $3d_{5/2}$ and Mo $3d_{3/2}$ which can be correlate with Mo^{+6} state in Bi_2MoO_6 [33]. Fig. 2d show the XPS high resolution spectra for O 1s. The wide asymmetric O 1s peak can be deconvoluted into three component peaks at 528.9 eV, 529.2 eV and 530.2 eV which can be assign to Bi-O, Mo-O and C-OH, respectively [34]. The latter two peaks could be indexed to O^{2-} lattices in Bi_2MoO_6 with OH group on the surface of the sample [35]. The Cd 3d orbit scan with two characteristics peak located at 402.9 eV and 409.7 eV, which can be assign to Cd $3d_{5/2}$ and Cd $3d_{3/2}$ for Cd^{2+} state in Bi_2MoO_6/CdS heterostructures (Fig. 2e) [36]. Figure 2f shows the XPS peak for S 2p located at 159.3 eV and 160.5 eV, corresponding to S^{2-} in CdS and Bi_2MoO_6/CdS heterostructures [37]. It can be concluded from the XPS analysis that the Bi_2MoO_6 deposited on the surface of CdS nanobelts in Bi_2MoO_6/CdS heterostructures nanocomposite. Structure and morphology of Bi_2MoO_6/CdS hetero-structures

The morphology and crystal structures of the samples was based on SEM and TEM images. Fig. 3a present the SEM image of Bi_2MoO_6. It can be seen that the Bi_2MoO_6 prepared by hydrothermal method crystalized in the form of microspheres with diameter ranges from 1-3 μm. Fig. 3b is the TEM images of CdS nanobelts. The results show that the CdS presents belt shape morphology which are 35-60 nm in thickness, 115-280 nm in width and 1-12 micrometer in length [38]. Such morphology can provide large surface area and abundant nucleation sites for the deposition of Bi_2MoO_6. Fig. 3c is present the SEM image of Bi_2MoO_6/CdS heterostructures nanocomposite (ratio= 3:1), which show that the surface of CdS nanobelts is homogeneously covered with Bi_2MoO_6 microspheres. Thus, results a morphology with large specific surface area. Moreover, such kind of morphology can provide large surface for reactive species and can act as a fast charge transfer channel. Fig. 3 d-j is the corresponding EDS elemental mapping images for Bi_2MoO_6/CdS heterostructures nanocomposite (raio=3:1), with Bi, Mo, O, Cd and S elements are found in the sample and no impurities observed in the EDS elemental mapping.

Fig. 4a is the TEM image of CdS nanobelts. It can be seen that the CdS crystallized in the form of nanobelt with diameter ~230 nm, which agrees well with the SEM image for CdS nanobelts (Fig. 3b). The belt shaped morphology can provide large surface if used a templet material for deposition of another substrate. Fig. 4b and c is the TEM images of Bi_2MoO_6/CdS heterostructures (ratio= 3:1). It can be seen that the Bi_2MoO_6 deposited in the form of nanosheets over the surface of CdS nanobelts. A very thin layer of Bi_2MoO_6 homogeneously covered the CdS nanobelts can be seen in Fig. 4c resulting in three-dimensional (3D) morphology. Furthermore, the CdS nanobelts remains the same belt shape morphology after the deposition of Bi_2MoO_6 nanosheets. The TEM images of Bi_2MoO_6/CdS heterostructures with different mole ratios are presented in Fig. S4. Fig. 4d is the corresponding EDS spectra of Bi_2MoO_6/CdS heterostructures. The elements such as Bi, Mo, O, Cd and S are observed in the EDS spectra for as prepared sample. No further impurities can be seen in the EDS spectra. The as prepared heterostructures nanocomposite could provide a fast charge transfer in Bi_2MoO_6/CdS heterostructures and efficient charge separation compare to Bi_2MoO_6 and CdS and hence can improve the photocatalytic activity.

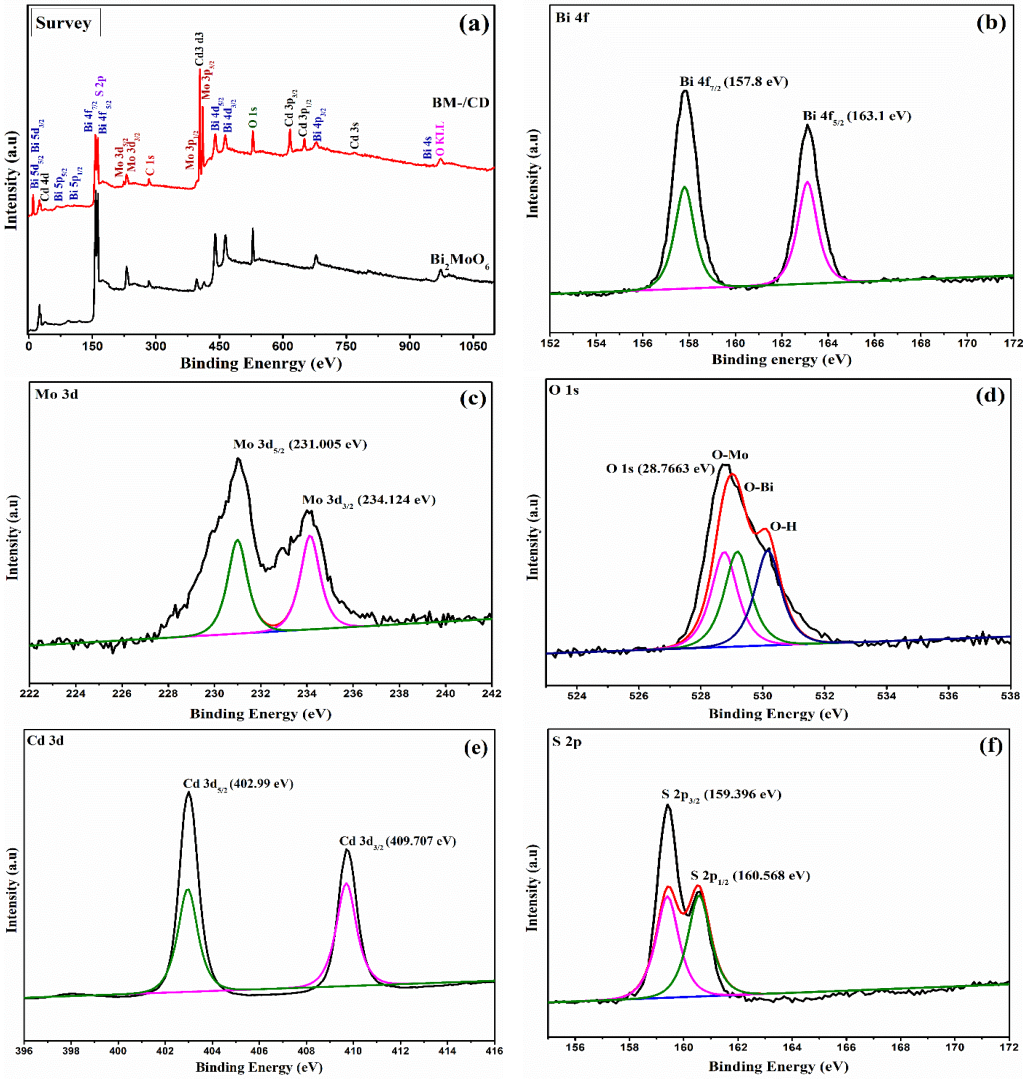

Fig. 2. High resolution XPS spectra of Bi_2MoO_6 and Bi_2MoO_6/CdS heterostructures.

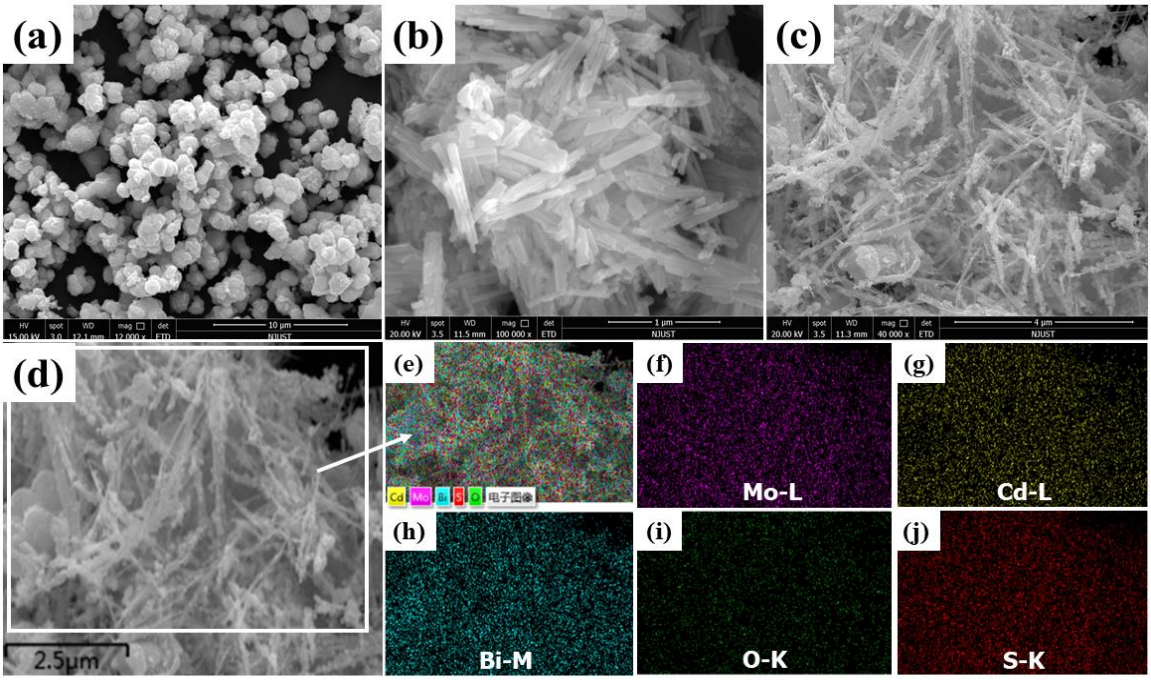

Fig. 3. SEM images (a) Bi_2MoO_6, (b) CdS nanobelts, (c) BM-3/CD, (d-j) corresponding EDS elemental mapping images of BM-3/CD for Bi, Mo, O, Cd and S.

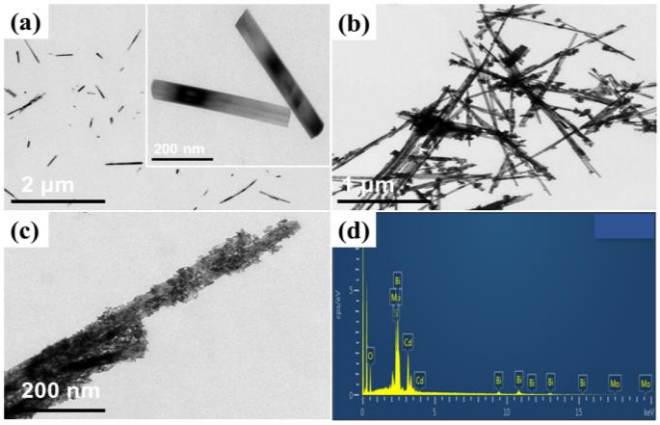

Fig. 4. TEM images of (a) CdS nanobelt, (b, c) BM-3/CD, (d) corresponding EDS spectrum of BM-3/CD.

B. Optical Properties of as-Prepared Samples

The photo-response properties of Bi_2MoO_6, CdS and Bi_2MoO_6/CdS heterostructures were measured and the results are displayed in Fig. 5a. The absorption of pure Bi_2MoO_6 nanosheet is located at 478 nm, which agrees precisely with bandgap energy of pure Bi_2MoO_6 [19]. However, the absorption of CdS is extended in the visible region at absorption edge to 617 nm. After growth of Bi_2MoO_6 on the surface of CdS nanobelt, the absorption of Bi_2MoO_6/CdS heterostructures is significantly enhanced in the visible region compare to pure Bi_2MoO_6, and the absorption edges located at 643 nm. The red shift in the absorption of Bi_2MoO_6 is mainly because of surface and morphological change from Bi_2MoO_6 to Bi_2MoO_6/CdS heterostructures nanocomposite. Eventually, such kind of surface and morphological changes and great enhancement in absorption would results in excessive improvement in the photocatalytic activity of Bi_2MoO_6/CdS heterostructures nanocomposite and effective exploitation of solar energy. Based on the absorption edges of Bi_2MoO_6, CdS and Bi_2MoO_6/CdS (inset of Fig. 5a), their bandgap energy calculated is 2.71 eV, 2.15 eV and 2.09 eV, respectively.

The separation efficiency of photogenerated charge carriers have been studied by photoluminescence (PL). It is known that the higher the photoluminescence emission intensity, the higher is the recombination of photogenerated charge carriers. The photoluminescence spectra of Bi_2MoO_6, CdS and Bi_2MoO_6/CdS heterostructures nanocomposite samples was investigated and the results are displayed in Fig. 5b. The Bi_2MoO_6 and CdS exhibit strong photo-emission peak at 455 nm which is due to the intrinsic photoluminescence properties of Bi_2MoO_6 [39]. Compare to Bi_2MoO_6, the CdS show slightly weaker emission peak which can be infer that the separation of photoexcited charge carriers efficiency of CdS is better than Bi_2MoO_6 [40]. The photoluminescence emission intensity of Bi_2MoO_6/CdS heterostructures is much lower compare to pure Bi_2MoO_6 and CdS nanobelts. This indicate that the Bi_2MoO_6/CdS heterostructures can efficiently suppress the recombination of photogenerated electrons-holes and eventually can enhance the photocatalytic activity.

C. BET Specific Surface Area and Pore Size Distribution

Fig. 6 presents the nitrogen adsorption-desorption isotherms at 77 K for Bi_2MoO_6, CdS and Bi_2MoO_6/CdS heterostructures nanocomposite and the inset is the pore size distribution by BJH method, respectively. The obtained results show all the three samples are similar and the nitrogen adsorption-desorption isotherms are type IV with hysteresis loops according to IUPAC classification [41], which signifying the existence of mesopores. Furthermore, the rapid increase of isotherms adsorption branches at relative pressure near to unity, indicating some resemblance with type II isotherms, which indicates the presence of macropores in the samples. All the hysteresis loops can be considered as type H3, indicating the presence of slit-like pores. The BET data are summarized in Table I, specifying the specific surface areas, pore volume and average pore size of the samples. The BET specific surface area (S_{EBT}) for CdS, Bi_2MoO_6 and Bi_2MoO_6/CdS heterostructures nanocomposite is 10.4 $m^2 g^{-1}$, 30.7 $m^2 g^{-1}$ and 52.7 $m^2 g^{-1}$, respectively. The specific surface area for Bi_2MoO_6/CdS heterostructures nanocomposite is larger than the pure Bi_2MoO_6 and CdS nanobelts. The variation in the specific surface area can also affect the pore size distribution. The inset of Fig. 6 show that the CdS nanobelts contains mesopores (3-35 nm) and macropores (35-97 nm), while the pore size distribution changes after the deposition of Bi_2MoO_6 over the surface of CdS nanobelts in B_2MoO_6/CdS which is 2-46 nm mesopores and 46-284 nm macropores, respectively. The deposition of Bi_2MoO_6 over the surface of CdS can introduce a lot of mesopores and macropores, while the number of mesopores quite increased in Bi_2MoO_6/CdS heterostructures. Consequently, decrease the average pore size from 40.7 nm (CdS nanobelts) to 26.45 nm (Bi_2MoO_6/CdS heterostructures). Thus, results in the large specific surface area of Bi_2MoO_6/CdS heterostructures nanocomposite.

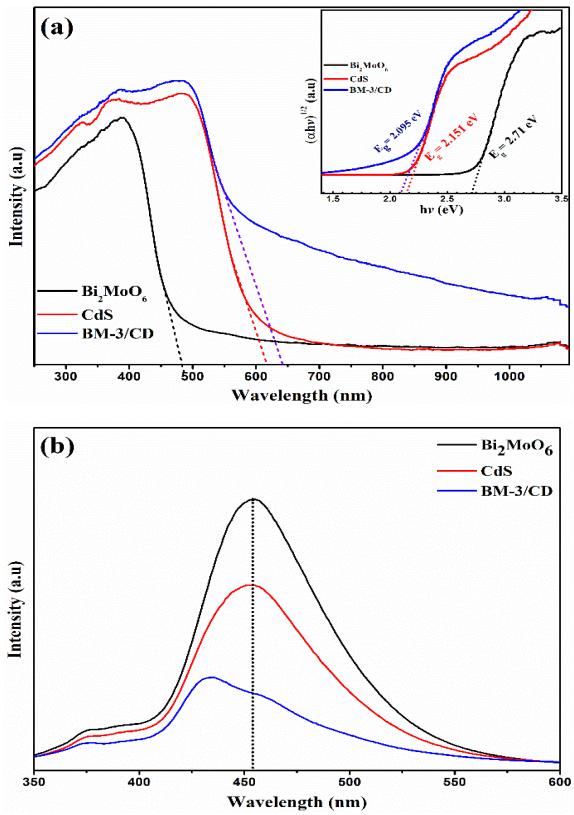

Fig. 5. (a) UV/vis DRS of Bi_2MoO_6, CdS and BM-3CD, (b) Photoluminescence (PL) spectra of Bi_2MoO_6, CdS and BM-3/CD heterostructures (λ_{ex}= 331 nm).

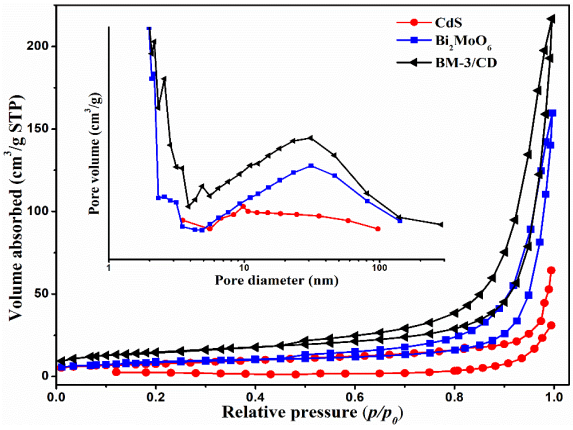

Fig. 6. Nitrogen adsorption-desorption isotherms for Bi_2MoO_6, CdS nanobelts and Bi_2MoO_6/CdS heterostructures nanocomposite calculated at BJH method. The inset is the corresponding pore size distributions.

TABLE I: EFFECT OF SPECIFIC SURFACE AREA ON PHOTOCATALYTIC ACTIVITIES OF SAMPLES

samples	S_{BET} ($m^2 g^{-1}$)	pore volume ($cm^3 g^{-1}$)	average pore size (nm)	activity (mmol h^{-1} g^{-1})	% deg/40 min (RhB)
CdS	10.4	0.020	40.7	0.146	63
Bi_2MoO_6	30.8	0.125	29.5	0.299	37
BM-3/CD	52.7	0.189	26.4	0.773	100

D. Photocatalytic Decomposition of Colored/Colorless Organic Pollutants

The photocatalytic performance of Bi_2MoO_6/CdS heterostructures nanocomposite have been performed for the degradation of rhodamine B and phenol under visible light irradiation. Bi_2MoO_6 and CdS have been used as reference under the same experimental condition (Fig. 7). Before irradiation, the sample were stirred in dark for 30 min to attain the adsorption equilibrium. A blank experiment was measured and neglected before visible light irradiation. The obtained results show that the Bi_2MoO_6/CdS heterostructures nanocomposite performed enhanced photocatalytic degradation under visible light irradiation. Fig. 7a, b show that the photocatalytic activity of Bi_2MoO_6 is lower than CdS nanobelts and Bi_2MoO_6/CdS heterostructures. The reason can be attributed to its wide bandgap which can utilize a very small portion of visible light. After the deposition of Bi_2MoO_6 over the surface of CdS nanobelts, the photocatalytic performance of Bi_2MoO_6/CdS much more increased compare to Bi_2MoO_6 and CdS nanobelts. It can be seen (Fig. 7a, b) that the photodegradation performance of Bi_2MoO_6/CdS heterostructure reaches to 100% in 40 min which is better than Bi_2MoO_6 (37%) and CdS (63%). The results can be inferring to the precise heterojunction between Bi_2MoO_6 and CdS which can facilitate faster photogenerated charge transfer from CB of CdS to CB of Bi_2MoO_6.

The photocatalytic performance of Bi_2MoO_6/CdS heterostructures with different mole ratios of Bi_2MoO_6 and CdS are also investigate and the results are shown in Fig. 7c. With increasing mole ratio of Bi_2MoO_6 and CdS, the photocatalysis performance of Bi_2MoO_6/CdS heterostructures are also increases. After a certain value (ratio= 3:1), the photocatalysis performance of Bi_2MoO_6/CdS achieve the highest photocatalytic activity and then decrease. The possible reasons are as follows: the Bi_2MoO_6 and CdS both can absorb visible light, after the deposition of Bi_2MoO_6 on the surface of CdS nanobelts, the photoexcited electrons in the CB of CdS can be transferred to the CB of Bi_2MoO_6 and the photocatalytic performance hence improved. As increasing the mole ratios of Bi_2MoO_6 and CdS, the photocatalytic performance also increases (ratio= 2:1, 3:1), while the phtocatalytic performance achieves the highest at 3:1 and start decreasing at 4:1. This might be due to the high concentration of Bi_2MoO_6 over the surface of CdS nanobelts which covers the surface of CdS nanobelts from direct contact of visible light and hence can cover the active sits of CdS nanobelts, which can cause hindering the photoexcited electron transfer between the interface of CdS and Bi_2MoO_6, eventually causing poor photocatalytic activity. Furthermore, the deposition of large volume of Bi_2MoO_6 on the surface of CdS nanobelt have smaller specific surface area and the CdS nanobelts surface can be covered from visible light absorption.

To further explain the enhanced photocatalytic activity of Bi_2MoO_6/CdS heterostructures, the photocurrent response of Bi_2MoO_6 nanosheets, CdS nanobelts and Bi_2MoO_6/CdS heterostructures as a working electrode was investigated (Fig. 8). Under the same experimental condition, the photocurrent response of Bi_2MoO_6/CdS heterostructures nanocomposite is 3 times higher than Bi_2MoO_6 nanosheets (Fig. 8a). Furthermore, the photocurrent response of Bi_2MoO_6/CdS heterostructures is more stable after several times on/off light compare to pure Bi_2MoO_6 and CdS, respectively. The higher and stable photocurrent response of Bi_2MoO_6/CdS heterostructures electrode indicates the efficient charge generation under the stimulation of visible light and improved electron-hole separation of photoexcited charge carriers.

E. Photocatalytic Oxygen Evolution of Bi_2MoO_6/CdS Heterostructures Nanocomposite

The photocatalytic activity of Bi_2MoO_6, CdS and Bi_2MoO_6/CdS heterostructures nanocomposite was also investigated for oxygen evolution under visible light irradiation and the results are displayed in Fig. 9. According to the previous literature, the valence band potential of both Bi_2MoO_6 (2.39 eV) and CdS (1.68 eV) are more positive than the typical redox potential of H_2O/O_2 (1.23 eV vs. RHE at pH= 0), which indicate that the hole generated during photoexcitation of Bi_2MoO_6, CdS and Bi_2MoO_6/CdS could oxidize H_2O to yield O_2 [42]. Under visible light excitation, the Bi_2MoO_6 and CdS show poor photocatalytic oxygen evolution. The photocatalytic oxygen evolution activity of Bi_2MoO_6 is higher than CdS nanobelts; the reason could be attributed to the fast electron-hole recombination of photoexcited charge carriers of CdS nanobelt or possibly due to the photocorrosion of CdS nanobelt under visible light illumination, which can oxidize the sulphur by photogenerated hole before water oxidation. Although, the Bi_2MoO_6/CdS heterostructures show the highest oxygen evolution activity (0.773 mmol h^{-1} g^{-1}) compare to Bi_2MoO_6 and CdS which is 0.299 mmol h^{-1} g^{-1} and 0.146 mmol h^{-1} g^{-1} (Fig. 9a). Fig. 9b show the oxygen evolution activity of Bi_2MoO_6/CdS with different mole ratios of Bi_2MoO_6 and

CdS. It can be seen that the oxygen evolution activity is increasing with increasing the mole ratio of Bi_2MoO_6 and achieve the highest O_2 evolution of 0.773 mmol h^{-1} g^{-1} (ratio= 3:1) and then start decreasing (ratio= 4:1); the reason might be because of high aggregates of Bi_2MoO_6 on the surface of CdS nanobelts which can prevent the CdS nanobelts from direct contact of visible light. The effective oxygen evolution activity can be attributed to the strong heterojunction between Bi_2MoO_6 and CdS nanobelt which can facilitate the charge transfer and suppress the rate of photoexcited electrons/holes recombination, eventually causing improved photocatalytic oxygen evolution.

F. Active Reactive Species Test

During the photocatalytic activity, the photocatalytic active oxidative species such as super oxide ($\bullet O^{2-}$), holes (h^+) and hydroxyl radicles (•OH) will be produced with powerful oxidation ability. To determine the active species generated during the photoexcitation of Bi_2MoO_6/CdS heterostructures, the active species trapping experiments was performed. The sacrificial agents, such as isopropyl alcohol (IPA), 1, 4-benzoquinone (BQ) and ethylene diaminetetraacetet (EDTA) were used as quenchers for $\bullet O^{2-}$, h^+ and •OH, respectively [43], [44]. It can be seen in Figure 8b, the photocatalytic activity of Bi_2MoO_6/CdS was slightly affected by the addition of IPA, indicating that the hydroxy radicles (•OH) to some extent play active role in the degradation of pollutants. However, the photocatalytic activity of Bi_2MoO_6/CdS significantly decreased by addition of BQ and EDTA, indicating that the $\bullet O^{2-}$ and h^+ are the main active species and play important role in the pollutants degradation.

G. Photocatalytic Mechanism for Bi_2MoO_6/CdS Heterostructures Nanocomposite

It is well-known that photocatalytic activity of materials can be improved by large specific surface area, thus could provide more surface area for O_2 absorption [45]. The improved photocatalysis performance of Bi_2MoO_6/CdS can be ascribed to the following reasons: first, the DRS analysis (Fig. 5a) shows that the Bi_2MoO_6/CdS heterostructures has a narrow bandgap (2.09 eV) can efficiently absorb visible light compare to Bi_2MoO_6, consequently enhance the photocatalytic performance. Secondly, the specific surface area of Bi_2MoO_6/CdS heterostructure nanocomposite (52.8 m^2 g^{-1}) is larger than the Bi_2MoO_6 (30.7 m^2 g^{-1}) and CdS nanobelt (10.4 m^2 g^{-1}). The large surface area of Bi_2MoO_6/CdS heterostructures nanocomposite not only enhance the visible light absorption, but also can enhance the separation of photogenerated charge carriers and provide larger surface area for RhB absorption, thus can enhance the photocatalytic performance. Furthermore, the photocurrent response and PL results (Fig. 8a and Fig. 5b) of Bi_2MoO_6/CdS indicates the high charge mobility and effective separation of photogenerated electrons/holes, which is beneficial for enhance photocatalysis and photostability of Bi_2MoO_6/CdS heterostructures. Consequently, the Bi_2MoO_6/CdS heterostructures nanocomposite can enhance the visible light absorption, efficiently promote the photogenerated charge carriers and can effectively suppress the electron/holes recombination which finally results in close contact between pollutants and photocatalyst, hence improve the photocatalytic activity.

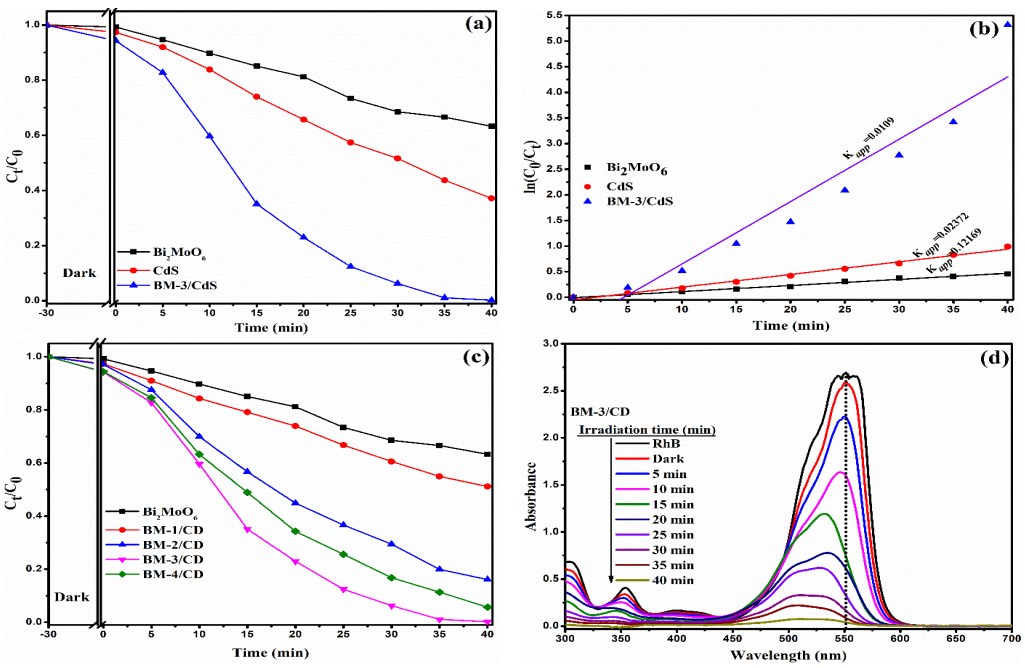

Fig. 7. (a) Photocatalytic decomposition of RhB for Bi_2MoO_6, CdS and Bi_2MoO_6/CdS heterostructures under visible light irradiation ($\lambda \geq 420$ nm), (b) plot of $\ln C_0/C_t$ verses time spectra, (c) comparison of photocatalytic performance of Bi_2MoO_6/CdS with different mole ratios, (d) absorbance spectra of Bi_2MoO_6/CdS heterostructures (ratio= 3:1).

On the bases of above discussion and active species trapping experiment, the possible mechanism for photocatalytic degradation and water oxidation was supposed and displayed in Fig. 10 scheme 1 and 2. The CB band potential of Bi_2MoO_6 and CdS are -0.32 eV and -0.4 eV, whereas the VB band are 2.39 eV and 1.68 eV [46]. The experimental bandgap for Bi_2MoO_6 and CdS are calculates as 2.71 eV and 2.15 eV, while for Bi_2MoO_6/CdS heterostructures nanocomposite the bandgap energy of 2.09 eV have been achieved (inset of Figure 5a). Under visible

light irradiation, both the Bi_2MoO_6 and CdS can be excited and the photogenerated electron and hole could be generates in CB and VB of Bi_2MoO_6 and CdS, respectively. As the CB band of CdS is more negative than the Bi_2MoO_6 while the VB band of Bi_2MoO_6 is more positive than the VB band of CdS, the photoexcited electron in CB of CdS can easily migrate to CB of Bi_2MoO_6, while the holes could be migrating from VB of Bi_2MoO_6 to VB of CdS. Due to strong interfacial contact between Bi_2MoO_6 and CdS in Bi_2MoO_6/CdS heterostructures, the photogenerated electrons/holes could efficiently migrate between Bi_2MoO_6 and CdS which results in effective separation of photogenerated charge carriers. Furthermore, the CB band potential of Bi_2MoO_6 (-0.32 eV) is more negative than the standard redox potential of ($E(O_2/\bullet O_2^-)$= 0.046 eV vs NHE) [47], which indicates that the photogenerated electrons in the CB of Bi_2MoO_6 could be captured by O_2 to produce $\bullet O_2^-$ radicles [48]. Likewise, the VB band of CdS (1.68 eV) is less positive than $E_0(\bullet OH/OH^-$ = 2.38 eV) [49] indicating that the h^+ in the VB of CdS could not oxidize OH^- to produce •OH radicles and can directly decompose the pollutants (Fig. 10 scheme 1).

Based on the above discussion, the proposed reaction occurring in the photocatalytic degradation of RhB over Bi_2MoO_6/CdS heterostructures are as follow:

$$Bi_2MoO_6 \rightarrow Bi_2MoO_6(e^- + h^+) \quad (1)$$

$$CdS \rightarrow CdS(e^- + h^+) \quad (2)$$

$$Bi_2MoO_6(e^- + h^+) \rightarrow Bi_2MoO_6(e^-) + Bi_2MoO_6(h^+) \quad (3)$$

$$Bi_2MoO_6(e^-) + O_2 \rightarrow \bullet O_2^- \quad (4)$$

$$\bullet O_2^- + \text{organic pollutants} \rightarrow \text{degradation products} \quad (5)$$

$$CdS(e^- + h^+) \rightarrow CdS(e^-) + CdS(h^+) \quad (6)$$

$$CdS(h^+) + \text{organic pollutants} \rightarrow \text{degradation products} \quad (7)$$

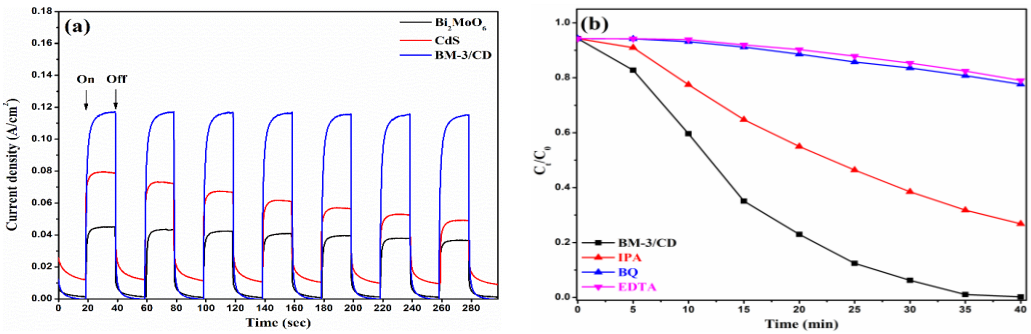

Fig. 8. (a) Photocurrent response of Bi_2MoO_6, CdS and Bi_2MoO_6/CdS heterostructures, (b) photocatalytic degradation of RhB over Bi_2MoO_6/CdS heterostructures (ratio= 3:1) with different scavengers.

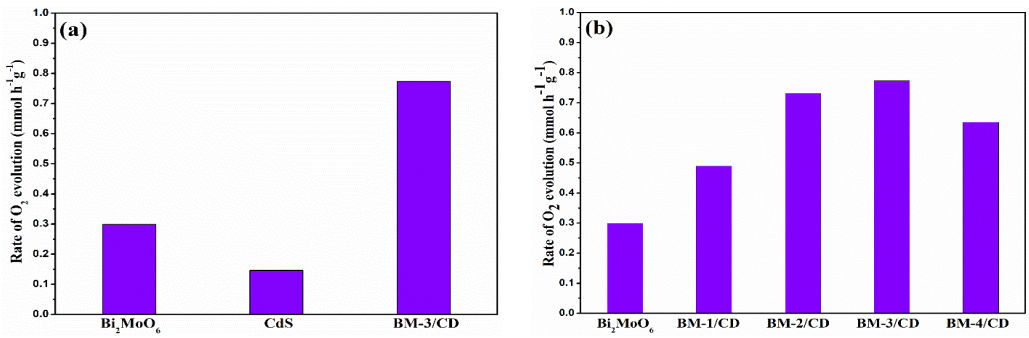

Fig. 9. (a) Photocatalytic oxygen evolution activity of Bi_2MoO_6, CdS and Bi_2MoO_6/CdS heterostructures under visible light irradiation ($\lambda \geq$ 420 nm), (b) comparison of photocatalytic oxygen evolution performance of Bi_2MoO_6/CdS with different mole ratios.

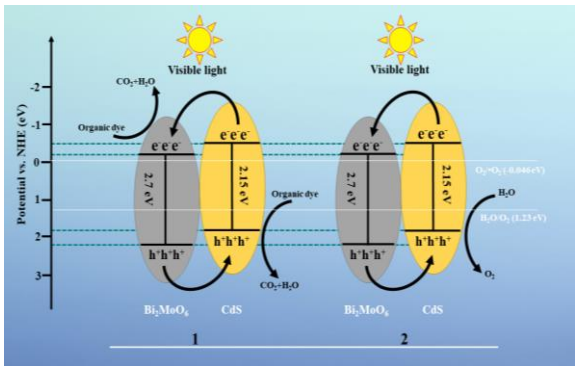

Fig. 10. Schematic photocatalytic mechanism of Bi_2MoO_6/CdS heterostructures for pollutant degradation (1) and water oxidation (2) under visible light irradiation.

Keeping in mind, that the VB band potential of CdS (1.68 eV) is more positive than the standard redox potential of H_2O/O_2 (1.23 eV vs RHE at pH= 0) [47], this indicate that the photogenerated holes in VB of CdS could oxidize the H_2O to yield O_2 [50]. In the case of water oxidation, the photogenerated electrons in the CB of CdS could migrate and accumulate in the CB of Bi_2MoO_6 while the residual holes in the VB of CdS may able to react with H_2O to generate active •OH (Eq= 9) and hence can oxidize the water molecule to produce oxygen (Figure 10 scheme 2) [51].

$$CdS(e^- + h^+) \rightarrow CdS(e^-) + CdS(h^+) \quad (8)$$

$$CdS(h^+) + H_2O \rightarrow H^+ + \bullet OH \quad (9)$$

On the bases of above discussion, the enhanced photocatalytic performance of Bi_2MoO_6/CdS heterostructures can be attributed to the large specific surface

area, efficient photogeneration of electrons/holes and effective separation of photogenerated charge carriers during the photocatalytic degradation of pollutant and photooxidation of water to yield O_2. Furthermore, the large specific surface area of Bi_2MoO_6/CdS heterostructures nanocomposite provides more active sites for photocatalytic reaction, which can remarkably enhance and enlarge the reaction space.

IV. Conclusions

In this work, we synthesis 3D Bi_2MoO_6/CdS heterostructures nanocomposite via two steps simple hydrothermal method. Bi_2MoO_6 were loaded on the surface of 1D CdS nanobelt to make Bi_2MoO_6/CdS heterostructures. The as prepared photocatalyst possess large specific surface area, high charge mobility and efficient separation of photogenerated charge carriers. Importantly, the as prepared photocatalyst show enhanced photocatalytic degradation of organic pollutants and water oxidation for O_2 evolution. Moreover, the heterostructures also exhibits excellent photoelectrochemical performance and efficient photocatalytic stability. The enhanced photocatalytic activity and photostability can be attributed to large specific surface area, porous morphology, efficient charge mobility, charge separation, retard photogenerated electrons/holes pairs. All the experimental results indicate a strong heterojunction of Bi_2MoO_6 and CdS nanobelt in Bi_2MoO_6/CdS heterostructures nanocomposite. We demonstrate that the heterostructures photocatalyst has a great potential for photocatalytic application.

Acknowledgment

The corresponding author wish to acknowledge the financial support by the National Natural Science Foundation of China (grant no. 51572126), and the Doctor Discipline Special Research Foundation of Chinese Ministry of Education (grant no. 20133219110015).

References

[1] M. Long, W. Cai, J. Cai, B. Zhou, X. Y. A. Chai, and W. Yahui, "Efficient photocatalytic degradation of phenol over Co_3O_4/$BiVO_4$ composite under visible light irradiation," *J. Phys. Chem. B.*, vol. 110, pp. 20211-20216, 2006.

[2] Q. Xiang, J. Yu, and M. Jaroniec, "Nitrogen and sulfur co-doped TiO_2 nanosheets with exposed {001} facets: Synthesis, characterization and visible-light photocatalytic activity," *Phys. Chem. Chem. Phys.*, vol. 13, pp. 4853-4861, 2011.

[3] A. Ramchiary and S. K. Samdarshi, "Ag deposited mixed phase titania visible light photocatalyst – Superiority of Ag-titania and mixed phase titania co-junction," *Appl. Surf Sci.*, vol. 305, pp. 33-39, 2014.

[4] W. Cui, H. Wang, L. Liu, Y. Liang, and J. G. McEvoy, "Plasmonic Ag@AgCl-intercalated $K_4Nb_6O_{17}$ composite for enhanced photocatalytic degradation of Rhodamine B under visible light," *Appl. Surf Sci.*, vol. 283, pp. 820-827, 2013.

[5] H. Tong, S. Ouyang, Y. Bi, N. Umezawa, M. Oshikiri, and J. Ye, "Nano-photocatalytic materials: Possibilities and challenges," *Adv. Mater*, vol. 24, pp. 229-251, 2012.

[6] L. Zou, H. Wang, and X. Wang, "High efficient photodegradation and photocatalytic hydrogen production of CdS/$BiVO_4$ heterostructure through *Z*-Scheme process," *ACS Sustain Chem. Eng.*, vol. 5, pp. 303-309, 2017.

[7] Y. Wang, X. Bai, C. Pan, J. He, and Y. Zhu, "Enhancement of photocatalytic activity of Bi_2WO_6 hybridized with graphite-like C_3N_4," *J. Mater Chem.*, vol. 22, pp. 11568-11573, 2012.

[8] F. X. Xiao, S. F. Hung, J. Miao, H. Y. Wang, H. Yang, and B. Liu, "Metal-cluster-decorated TiO_2 nanotube arrays: A composite heterostructure toward versatile photocatalytic and photoelectrochemical applications," *Small*, vol. 11, pp. 554–567, 2015.

[9] Z. Li, F. Wang, A. Kvit, and X. Wang, "Nitrogen doped 3D titanium dioxide nanorods architecture with significantly enhanced visible light photoactivity," *J. Phys. Chem. C*, vol. 119, pp. 4397-4405, 2015.

[10] L. Wang and T. Sasaki, "Titanium oxide nanosheets: Graphene analogues with versatile functionalities," *Chem. Rev*, vol. 114, pp. 9455-9486, 2014.

[11] S. Meng, X. Ye, X. Ning, M. Xie, X. Fu, and S. Chen, "Selective oxidation of aromatic alcohols to aromatic aldehydes by BN/metal sulfide with enhanced photocatalytic activity," *Appl. Catal. B Environ*, vol. 182, pp. 356-368, 2016.

[12] L. Kong, Z. Li, S. Huang, J. Jia, and L. Li, "Boosting photocatalytic performance and stability of $CuInS_2$/ZnS-TiO_2 heterostructures via sol-gel processed integrate amorphous titania gel," *Appl. Catal. B Environ*, vol. 204, pp. 403-410, 2017.

[13] I. Majeed, M. A. Nadeem, M. Al-Oufi *et al.*, "On the role of metal particle size and surface coverage for photo-catalytic hydrogen production: A case study of the Au/CdS system," *Appl. Catal. B Environ*, vol. 182, pp. 266-276, 2016.

[14] W. Wei, Y. Dai, and B. Huang, "First-principles characterization of Bi-based photocatalysts: $Bi_{12}TiO_{20}$, $Bi_2Ti_2O_7$, and $Bi_4Ti_3O_{12}$," *J. Phys. Chem. C*, vol. 113, pp. 5658-5663, 2009.

[15] G. Tian, Y. Chen, R. Zhai *et al.*, "Hierarchical flake-like Bi_2MoO_6/TiO_2 bilayer films for visible-light-induced self-cleaning applications," *J. Mater Chem. A*, vol. 1, pp. 6961-6968, 2013.

[16] Y. Huang, Z. Ai, W. Ho, M. Chen, and S. Lee, "Ultrasonic spray pyrolysis synthesis of porous Bi_2WO_6 microspheres and their visible-light-induced photocatalytic removal of NO," *J. Phys. Chem. C*, vol. 114, pp. 6342-6349, 2010.

[17] L. Zhang, W. Wang, L. Zhou, and H. Xu, "Bi_2WO_6 nano- and microstructures: Shape control and associated visible-light-driven photocatalytic activities," *Small*, vol. 3, pp. 1618–1625, 2007.

[18] C. Zhang and Y. Zhu, "Synthesis of square Bi_2WO_6 nanoplates as high-activity visible-light-driven photocatalysts," *Chem. Mater*, vol. 17, pp. 3537-3545, 2005.

[19] Y. Shimodaira, H. Kato, H. Kobayashi, and A. Kudo, "Photophysical properties and photocatalytic activities of bismuth molybdates under visible light irradiation," *J. Phys. Chem. B*, vol. 110, 17790-17797, 2006.

[20] Y. Fu, C. Chang, P. Chen, X. Chu, and L. Zhu, "Enhanced photocatalytic performance of boron doped Bi_2WO_6 nanosheets under simulated solar light irradiation," *J. Hazard Mater*, vol. 254, no. 255, pp. 185–192, 2013.

[21] H. Fu, S. Zhang, T. Xu, Y. Zhu, and J. Chen, "Photocatalytic degradation of RhB by fluorinated Bi_2WO_6 and distributions of the intermediate products," *Environ Sci. Technol.*, vol. 42, pp. 2085–2091, 2008.

[22] M. Ge, Y. Li, L. Liu, Z. Zhou, and W. Chen, "Bi_2O_3−Bi_2WO_6 composite microspheres: Hydrothermal synthesis and photocatalytic performances," *J. Phys. Chem. C*, vol. 115, pp. 5220–5225, 2011.

[23] L. Ge, C. Han, and J. Liu, "Novel visible light-induced g-C_3N_4/Bi_2WO_6 composite photocatalysts for efficient degradation of methyl orange," *Appl. Catal. B Environ*, vol. 108, no. 109, pp. 100–107, 2011.

[24] X. Meng, L. Jiang, W. Wang, and Z. Zhang, "Enhanced photocatalytic activity of BiOBr/ZnO heterojunction semiconductors prepared by facile hydrothermal method," *Int. J. Photoenergy*, pp. 1-9, 2015.

[25] X. Meng and Z. Zhang, "Synthesis, analysis, and testing of BiOBr-Bi_2WO_6 photocatalytic heterojunction semiconductors," *Int. J. Photoenergy*, pp. 1-12, 2015.

[26] M. Arif, Q. Li, J. Yao, T. Huang *et al.*, "Enhance photocatalysis performance and mechanism of CdS and Ag synergistic co-catalyst supported on mesoporous g-C_3N_4 nanosheets under visible-light irradiation," *J. Environ Chem. Eng.*, vol. 5, pp. 5358–5368, 2017.

[27] N. Bao, L. Shen, T. Takata, and K. Domen, "Self-templated synthesis of nanoporous CdS nanostructures for highly efficient photocatalytic hydrogen production under visible light," *Chem. Mater*, vol. 20, pp. 110–117, 2008.

[28] A. Kudo and Y. Miseki, "Heterogeneous photocatalyst materials for water splitting," *Chem. Soc. Rev*, vol. 38, pp. 253-278, 2009.

[29] X. F. Gao, W. T. Sun, Z. D. Hu, G. Ai *et al.*, "An efficient method to form heterojunction CdS/TiO_2 photoelectrodes using highly ordered TiO_2 nanotube array films," *J. Phys. Chem. C*, vol. 113, pp. 20481–20485, 2009.

[30] L. Zou, X. Wang, X. Xu, and H. Wang, "Reduced graphene oxide wrapped CdS composites with enhanced photocatalytic performance and high stability," *Ceram Int.*, vol. 42, pp. 372–378, 2016.

[31] J. S. Jang, U. A. Joshi, and J. S. Lee, "Solvothermal synthesis of CdS nanowires for photocatalytic hydrogen and electricity production," *J. Phys. Chem. C*, vol. 111, pp. 13280–13287, 2007.

[32] C. Sun, Q. Xu, Y. Xie, Y. Ling *et al.*, "High-efficient one-pot synthesis of carbon quantum dots decorating Bi_2MoO_6 nanosheets heterostructure with enhanced visible-light photocatalytic properties," *J. Alloys Compd*, vol. 5, no. 723, pp. 333-344, 2017.

[33] Z. Zhang, T. Zheng, J. Xu, H. Zeng, and N. Zhang, "Carbon quantum dots/Bi_2MoO_6 composites with photocatalytic H_2 evolution and near infrared activity," *J. Photochem. Photobiol. A*, vol. 346, pp. 24-31, 2017.

[34] L. Wang, M. Arif, G. Duan, S. Chen, and X. Liu, "A high performance quasi-solid-state supercapacitor based on $CuMnO_2$ nanoparticles," *J. Power Sources*, vol. 1, no. 355, pp. 53-61, 2017.

[35] C. Yu, Z. Wu, R. Liu *et al.*, "Novel fluorinated Bi_2MoO_6 nanocrystals for efficient photocatalytic removal of water organic pollutants under different light source illumination," *Appl. Catal. B*, vol. 15, no. 209, pp. 1-11, 2017.

[36] R. Zeng, R. Shen, Y. Zhao, X. Li, Z. Sun, and Y. Shen, "Aqueous synthesis of Cu-doped ZnCdS/ZnS core/shell nanocrystals with a new and highly reactive sulfur source," *Nanotechnology*, vol. 25, p. 135602, 2014.

[37] J. Yang, J. Wang, X. Li, D. Wang, and H. Song, "Synthesis of urchin-like Fe_3O_4@SiO_2@ZnO/CdS core–shell microspheres for the repeated photocatalytic degradation of rhodamine B under visible light," *Catal. Sci. Technol*., vol. 6, no. 12, pp. 4525-4534, 2016.

[38] J. Zhang, Y. Wang, J. Jin *et al.*, "Efficient visible-light photocatalytic hydrogen evolution and enhanced photostability of Core/Shell CdS/g-C_3N_4 nanowires," *ACS Appl. Mater Interfaces*, vol. 5, pp. 10317-0324, 2013.

[39] G. Tian, Y. Chen, J. Zhou *et al.*, "In situ growth of Bi_2MoO_6 on reduced graphene oxide nanosheets for improved visible-light photocatalytic activity," *Cryst. Eng. Comm.*, vol. 16, pp. 842-49, 2014.

[40] Y. Feng, X. Yan, C. Liu *et al.*, "Hydrothermal synthesis of CdS/Bi_2MoO_6 heterojunction photocatalysts with excellent visible-light-driven photocatalytic performance," *Appl. Surf. Sci.*, vol. 30, no. 353, pp. 87-94, 2015.

[41] D. Avnir and M. Jaroniec, "An isotherm equation for adsorption on fractal surfaces of heterogeneous porous materials," *Langmuir*, vol. 5, pp. 1431-1433, 1989.

[42] T. Jing, Y. Dai, W. Wei, X. Ma, and B. Huang, "Near-infrared photocatalytic activity induced by intrinsic defects in Bi_2MO_6 (M= W, Mo)," *Phys. Chem. Chem. Phys*., vol. 16, no. 34, pp. 18596-18604, 2014.

[43] X. Yan, G. Liu, L. Wang *et al.*, "Antiphotocorrosive photocatalysts containing CdS nanoparticles and exfoliated TiO_2 nanosheets," *J. Mater. Res*., vol. 25, no. 1, pp. 182-188, 2010.

[44] X. Chen, S. Shen, L. Guo, and S. S. Mao, "Semiconductor-based photocatalytic hydrogen generation," *Chem. Rev*, vol. 110, pp. 6503–6570, 2010.

[45] J. Cao, B. Xu, H. Lin, B. Luo, and S. Chen, "Novel heterostructured Bi_2S_3/BiOI photocatalyst: Facile preparation, characterization and visible light photocatalytic performance," *Dalt. Trans*, vol. 41, pp. 11482-11490, 2012.

[46] Y. Hong, A. Ren, Y. Jiang, J. He, L. Xiao, and W. Shi, "Sol–gel synthesis of visible-light-driven Ni(1−x)Cu(x)Fe_2O_4 photocatalysts for degradation of tetracycline," *Ceram Int*., vol. 41, pp. 1477-1486, 2015.

[47] B. Lu, X. Li, T. Wang, E. Xie, and Z. Xu, "WO_3 nanoparticles decorated on both sidewalls of highly porous TiO_2 nanotubes to improve UV and visible-light photocatalysis," *J. Mater Chem. A, vol.* 1, pp. 3900-3906, 2013.

[48] J. Long, S. Wang, H. Chang, B. Zhao, B. Liu, Y. Zhou *et al.*, "Bi_2MoO_6 Nanobelts for crystal facet-enhanced photocatalysis," *Small*, vol. 10, pp. 2791-2795, 2014.

[49] W. Shi, D. Du, B. Shen, C. Cui, L. Lu, L. Wang *et al.*, "Synthesis of Yolk–Shell structured Fe_3O_4@void@CdS nanoparticles: A general and effective structure design for photo-fenton reaction," *ACS Appl. Mater Interfaces*, vol. 8, pp. 20831–20838, 2016.

[50] S. Martha, A. Nashim, and K. M. Parida, "Facile synthesis of highly active gC_3N_4 for efficient hydrogen production under visible light," *J. Mater. Chem. A*, vol. 1, no. 26, pp. 7816-7824, 2013.

[51] H. Cheng, B. Huang, Y. Dai, X. Qin, X. Zhang, "One-Step synthesis of the nanostructured AgI/BiOI composites with highly enhanced visible-light photocatalytic performances," *Langmuir*, vol. 26, pp. 6618-6624, 2010.

Muhammad Arif is a PhD student in the School of Chemical Engineering, Nanjing University of Science and Technology, Nanjing, P. R. China. Recently his research work is mainly focused on photocatalysis, photocatalytic and photoelectrochemical water splitting and photoelectochemistry. From 2013 to 2015 he worked as a master student in Hazara University Mansehra Pakistan and as a research assistant in National Institute of Vacuum Science and Technology (NINVAST) Quaid-e-Azam University, NCP Complex, Islamabad, Pakistan.

Tong Yu is an undergraduate in materials chemistry at the Nanjing University of Science and Technology. Her current research focuses on the preparation and photocatalytic performance of BiOX (X=Cl, Br,I)/Au/CdS semiconductor composites

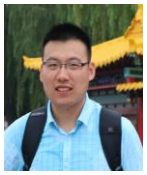

Min Zhang is a PhD in materials science and engineering at the Nanjing University of science and technology. His recent research focuses on applications of photocatalysis in Bi-based Oxysalt nanomaterials.

Qingyong Li is a PhD in materials science and engineering at the Nanjing University of Science and Technology. His recent research focused on applications of photocatalyst for environmental pollutants degradation.

Xiaoheng Liu is currently a professor of chemical engineering at the School of Chemical Engineering and Technology, Nanjing University of Science and Technology. Professor Liu work in a wide range of interdisciplinary experimental work within main theme of photocatalysis, photoelectochemistry and energy storage materials. Till to date, he published more than 200 scientific articles in various internationally renowned journals, technical papers, congress/conferences proceedings. He led numbers of projects which are funded by government organizations, industry and university.